

# Breaking Wave Interaction with a Vertical Cylinder and the Effect of Breaker Location

Arun Kamath<sup>1</sup>, Mayilvahanan Alagan Chella, Hans Bihs, Øivind A. Arntsen

*Department of Civil and Transport Engineering, Norwegian University of Science and Technology (NTNU), 7491 Trondheim, Norway*

---

## Abstract

The open-source CFD model REEF3D is used to simulate plunging breaking wave forces on a vertical cylinder. The numerical results are compared with data from the experiments carried out at the Large Wave Channel, Hannover, Germany to validate the model. Further, the location of the cylinder is changed so that the breaking wave impacts the cylinder at different stages of wave breaking and the resulting wave forces are evaluated. The different locations for the cylinder placement based on the breaker location are determined from the results obtained for the wave breaking process in a two-dimensional numerical wave tank. Maximum wave forces are found to occur when the breaking wave tongue impacts the cylinder just below the wave crest in all the cases simulated and the lowest wave forces are generally obtained when the wave breaks behind the cylinder. Several wave features such as the splashing on impact, the splitting and rejoining of the wave around the cylinder resulting in a chute-like jet formation are identified. The model provides a good representation of the breaking wave process and can be a useful tool to evaluate breaking wave forces on structures.

*Keywords:* breaking wave, wave forces, wave impact, vertical cylinder, Computational Fluid Dynamics, REEF3D

---

<sup>1</sup>Corresponding Author, Email: arun.kamath@ntnu.no, Ph: (+47) 73 59 46 40, Fax: (+47) 73 59 70 21

## 1. Introduction

A lot of research work has been carried out in the past on the evaluation of wave forces on structures exposed to waves due to their importance in coastal and offshore engineering. Wave interaction with a vertical circular cylinder depends on the Keulegan-Carpenter (KC) number and the relative size of the cylinder with respect to the incident waves. The KC number is a ratio between the excursion length of the fluid particles to the length of the obstacle in the flow. In the case of vertical circular cylinders in a wave field, it is given by  $KC = uT/D$ , where  $u$  is amplitude of the horizontal fluid velocity,  $T$  is the wave period and  $D$  is the diameter of the cylinder (Sumer and Fredsøe, 1997). The ratio measures the importance of the inertial forces and the drag forces. The wave forces on cylinders at higher KC numbers ( $KC > 2$ ) and cylinder diameter to wavelength ratio  $D/L < 0.2$  are generally determined using the Morison formula (Morison et al., 1950) to account for inertial and drag component of the wave forces using empirical force coefficients. In the case of breaking wave forces, the Morison formula cannot be directly applied because breaking waves are associated with impact forces of very high magnitudes acting over a short duration. In order to describe the total force from breaking waves with the Morison equation, an impact force term is considered in addition to the quasi-static forces (Goda et al., 1966). Present knowledge concerning the breaking wave forces is gained from experiments by Goda et al. (1966), Wienke and Oumeraci (2005), Arntsen et al. (2011) to name a few, but the measurement of velocity and acceleration under breaking waves and their interaction with structures is very demanding. The theoretical description of the impact force involves the use of several parameters such as slamming coefficients, curling factor, breaker shape and wave kinematics at breaking which have to be determined experimentally. Previous studies on breaking wave forces such as Chan and Melville (1988), Bullock et al. (2007), Wienke and Oumeraci (2005) have indicated that breaking wave impact characteristics depend on several parameters such as the depth inducing breaking, breaker type and the distance of the structure from

31 the breaker location.

32 The modelling of breaking waves in shallow waters is challenging due to  
33 the complex nature of the physical processes including highly non-linear inter-  
34 actions. A considerable amount of numerical studies have been attempted to  
35 model wave breaking over plane slopes (Lin and Liu, 1998; Zhao et al., 2004;  
36 Alagan Chella et al., 2015b). These studies have helped extend the knowl-  
37 edge regarding breaking wave characteristics and the geometric properties of  
38 breaking waves. The quantification of these breaking wave parameters are an  
39 important input to improve the empirical coefficients used for the evaluation of  
40 breaking wave forces. Though many extensive numerical studies exist in current  
41 literature that study the wave breaking process, not many have been extended  
42 to study the forces due to breaking waves and the effect of breaker types on  
43 the wave forces. Bredmose and Jacobsen (2010) studied breaking wave impact  
44 forces due to focussed waves with the Jonswap wave spectrum for input and  
45 carried out computations for half the domain assuming lateral symmetry of the  
46 problem using OpenFOAM. Mo et al. (2013) measured and modelled solitary  
47 wave breaking and its interaction with a slender cylinder over a plane slope for a  
48 single case using the filtered Navier-Stokes equations with large eddy simulation  
49 (LES) turbulence modeling, also assuming lateral symmetry and showed that  
50 their numerical model sufficiently captured the important flow features. Choi  
51 et al. (2015) investigated breaking wave impact forces on a vertical cylinder and  
52 two cases of inclined cylinders for one incident wave using the modified Navier-  
53 Stokes equations with the volume of fluid (VOF) method for interface capturing  
54 to study the dynamic amplification factor due to structural response.

55 The study of breaking wave forces using computational fluid dynamics (CFD)  
56 can provide a very detailed description of the physical processes as the fluid  
57 physics are calculated with few assumptions. With high-order discretization  
58 schemes for the convection and time advancement, sharp representation of the  
59 free surface and tight velocity-pressure coupling in the model, the wave trans-  
60 formation, wave hydrodynamics and flow features can be represented very accu-  
61 rately and in a realistic manner. In the complex case of breaking wave interac-

62 tion with structures, CFD simulations can be used to capture the details of the  
63 flow field that are challenging to capture in experimental studies due to various  
64 factors including cost, instrumentation and structural response. Different wave  
65 loading scenarios can be analysed as the breaker locations are easier to analyse  
66 and maintain in the simulations.

67 In the current study, the open source CFD model REEF3D (Bihs et al.,  
68 2016) is used to simulate periodic breaking wave forces on a slender cylinder in  
69 a three-dimensional wave tank without assuming lateral symmetry. The model  
70 has been previously used to simulate the wave breaking process under different  
71 conditions (Alagan Chella et al., 2015a,c) and the wave breaking kinematics  
72 were fully represented including the motion of the jet, air pocket formation and  
73 the reconnection of the jet with the preceding wave trough. The model provides  
74 a detailed representation of the free surface and is numerically stable for various  
75 problems related to wave hydrodynamics. It is fully parallelised, has shown very  
76 good scaling on the high performance computing system at NTNU provided by  
77 NOTUR (2012) and can be used to carry out complex simulations efficiently on  
78 a large number of processors.

79 This paper presents the breaking wave interaction with a vertical cylinder.  
80 Three different wave heights are simulated and the evolution of wave breaking  
81 over a 1 : 10 slope is studied using two-dimensional simulations. The locations  
82 for the placement of the cylinder to investigate five different wave loading cases  
83 based on Irschik et al. (2002) are identified from these two-dimensional studies.  
84 Next, the wave forces in the different scenarios for the three different incident  
85 wave heights are evaluated in a three-dimensional numerical wave tank. The  
86 numerical model is validated by comparing the calculated wave forces and the  
87 free surface with experimental data from experiments carried out in the Large  
88 Wave Channel (GWK), Hannover, Germany. The wave interaction with the  
89 vertical cylinder in selected two different scenarios is investigated and the effect  
90 of the cylinder placement with respect to the breaker location on the free surface  
91 features is presented.

92 **2. Numerical Model**

93 The open-source CFD model REEF3D solves the fluid flow problem using  
 94 the incompressible Reynolds-Averaged Navier-Stokes (RANS) equations along  
 95 with the continuity equation:

$$\frac{\partial u_i}{\partial x_i} = 0 \quad (1)$$

$$\frac{\partial u_i}{\partial t} + u_j \frac{\partial u_i}{\partial x_j} = -\frac{1}{\rho} \frac{\partial p}{\partial x_i} + \frac{\partial}{\partial x_j} \left[ (\nu + \nu_t) \left( \frac{\partial u_i}{\partial x_j} + \frac{\partial u_j}{\partial x_i} \right) \right] + g_i \quad (2)$$

96 where  $u$  is the velocity averaged over time  $t$ ,  $\rho$  is the fluid density,  $p$  is the  
 97 pressure,  $\nu$  is the kinematic viscosity,  $\nu_t$  is the eddy viscosity and  $g$  is the accel-  
 98 eration due to gravity.

99 The pressure is determined using Chorin’s projection method (Chorin, 1968)  
 100 and the resulting Poisson pressure equation is solved with a preconditioned  
 101 BiCGStab solver (van der Vorst, 1992). Turbulence modeling is handled using  
 102 the two-equation  $k - \omega$  model proposed by Wilcox (1994), where the transport  
 103 equations for the turbulent kinetic energy,  $k$  and the specific turbulent dissipa-  
 104 tion rate,  $\omega$  are:

$$\frac{\partial k}{\partial t} + U_j \frac{\partial k}{\partial x_j} = \frac{\partial}{\partial x_j} \left[ \left( \nu + \frac{\nu_t}{\sigma_k} \right) \frac{\partial k}{\partial x_j} \right] + P_k - \beta_k k \omega \quad (3)$$

$$\frac{\partial \omega}{\partial t} + U_j \frac{\partial \omega}{\partial x_j} = \frac{\partial}{\partial x_j} \left[ \left( \nu + \frac{\nu_t}{\sigma_\omega} \right) \frac{\partial \omega}{\partial x_j} \right] + \frac{\omega}{k} \alpha P_k - \beta \omega^2 \quad (4)$$

$$\nu_t = \frac{k}{\omega} \quad (5)$$

107 where,  $P_k$  is the production rate and closure coefficients  $\sigma_k = 2$ ,  $\sigma_\omega = 2$ ,  $\alpha =$   
 108  $5/9$ ,  $\beta_k = 9/100$ ,  $\beta = 3/40$ .

109 The highly strained flow due to the propagation of waves in the tank results  
 110 in an overproduction of turbulence in the numerical wave tank as the eddy  
 111 viscosity is determined from the strain in the convective terms. The Bradshaw  
 112 et al. (1967) assumption is used to limit the eddy viscosity as shown by Durbin

113 (2009):

$$\nu_t \leq \sqrt{\frac{2}{3}} \frac{k}{|\mathbf{S}|} \quad (6)$$

114 where  $\mathbf{S}$  stands for the source terms in the transport equations. In a two-phase  
115 CFD model, the large difference between the density of air and water leads to  
116 a large strain at the interface, which leads to an overproduction of turbulence  
117 at the free surface. In reality, the free surface is a boundary at which eddy  
118 viscosity is damped naturally which the standard  $k - \omega$  model does not account  
119 for. In order to avoid the overproduction of turbulence at the free surface, the  
120 specific turbulence dissipation at the free surface is defined using the empirical  
121 relationship presented by Naot and Rodi (1982).

122 The discretization of the convective terms of the RANS equations are dis-  
123 cretized using the fifth-order conservative finite difference Weighted Essentially  
124 Non-Oscillatory (WENO) scheme (Jiang and Shu, 1996). The Hamilton-Jacobi  
125 formulation of the WENO scheme (Jiang and Peng, 2000) is used to discretize  
126 the level set function  $\phi$ , turbulent kinetic energy  $k$  and the specific turbulent  
127 dissipation rate  $\omega$ . The WENO scheme is at minimum a third-order accu-  
128 rate scheme in the presence of large gradients and provides sufficient accuracy  
129 required to model complex free surface flows. The time advancement of the  
130 momentum equation, the level set function and the reinitialisation equation is  
131 treated with a Total Variation Diminishing (TVD) third-order Runge-Kutta ex-  
132 plicit time scheme (Shu and Osher, 1988). The Courant-Frederick-Lewis (CFL)  
133 criterion is maintained at a constant value throughout the simulation using an  
134 adaptive time stepping strategy to determine the time steps. A first-order im-  
135 plicit scheme for the time advancement of  $k$  and  $\omega$  removes the large source term  
136 contributions from these variables for the evaluation of the CFL criterion. This  
137 is reasonable, as these variables are largely driven by source terms and have a  
138 low influence from the convective terms. The diffusion terms of the velocities are  
139 also handled using an implicit scheme, removing them from the CFL criterion  
140 and the maximum velocities in the domain are used to determine the time steps  
141 to maintain the numerical stability of the simulation.

142 The model uses a Cartesian grid for spatial discretization and high-order  
143 finite difference schemes can be implemented in a straight forward manner. A  
144 ghost cell immersed boundary method (GCIBM) (Berthelsen and Faltinsen,  
145 2008) is used to account for the complex geometric solid-fluid boundaries. The  
146 code is fully parallelised using the MPI library and the numerical model can be  
147 executed on high performance computing systems with very good scaling.

### 148 *2.1. Level Set Method*

149 The level set method (Osher and Sethian, 1988) is an interface capturing  
150 method in which the the zero level set of a signed distance function,  $\phi(\vec{x}, t)$   
151 represents the interface between two phases. For the rest of the domain,  $\phi(\vec{x}, t)$   
152 gives the closest distance of each point in the domain from the interface and the  
153 sign distinguishes the two phases across the interface. The level set function is  
154 continuous across the interface and is defined as:

$$\phi(\vec{x}, t) \begin{cases} > 0 & \text{if } \vec{x} \text{ is in phase 1} \\ = 0 & \text{if } \vec{x} \text{ is at the interface} \\ < 0 & \text{if } \vec{x} \text{ is in phase 2} \end{cases} \quad (7)$$

155 The level set function provides a sharp representation of the interface. A partial  
156 differential equation based reinitialisation procedure presented by Peng et al.  
157 (1999) is used to maintain the signed distance property of the function, which  
158 can be lost on convecting the function under an external velocity field.

### 159 *2.2. Numerical Wave Tank*

160 The two-dimensional numerical wave tank has symmetry conditions on the  
161 side walls and the top of the tank. The bottom wall of the tank and boundaries of  
162 objects placed in the tank are treated with a no-slip or wall boundary condition.  
163 In a three-dimensional wave tank, the side walls are also subjected to wall  
164 boundary conditions. Wave generation is handled using the relaxation method  
165 (Larsen and Dancy, 1983), with the relaxation function presented by Jacobsen

166 et al. (2012):

$$\Gamma(x) = 1 - \frac{e^{(1-x)^{3.5}} - 1}{e - 1} \quad (8)$$

167 where  $\Gamma(x)$  is the relaxation function and  $x \in [0, 1]$  is the length scale along  
168 the relaxation zone and ensures a smooth transition of the still water to a wave.  
169 The relaxation function also absorbs any waves reflected from the objects placed  
170 in the wave tank, travelling towards the wave generation zone. This prevents  
171 the reflected waves from affecting the wave generation and simulates a wave  
172 generator with active absorption. The numerical beach is implemented using  
173 the active absorbing beach formulated by Schäffer and Klopman (2000).

### 174 **3. Results and Discussion**

#### 175 *3.1. Setup for the numerical simulations*

176 The experiments (Irschik et al., 2002) at the Large Wave Channel (GWK),  
177 Hannover are carried out in a wave channel 309 m long, 5 m wide and 7 m high  
178 with a 23 m long 1 : 10 slope reaching a height of 2.3 m placed at 180 m from  
179 the wavemaker. A flat bed extends from the end of slope with a height of 2.3 m.  
180 A vertical cylinder of diameter  $D = 0.7$  m is placed with its central axis at the  
181 top of the slope and incident waves with heights  $H$  between 1.15 – 1.60 m and  
182 periods  $T$  between 4.0 – 9.0 s are generated. In the current study, the case with  
183 incident wave period  $T = 4.0$  s, wave height  $H = 1.30$  m and water depth  $d = 3.8$   
184 m presented in Choi et al. (2015) is chosen for comparison with the numerical  
185 results. The three-dimensional numerical wave tank is 54 m long, 5 m wide and  
186 7 m high with a grid size of  $dx = 0.05$  m resulting a total of 15.12 million cells.  
187 In order to study the wave breaking process for the different cases simulated  
188 in the study, a two-dimensional wave tank with the same length and height is  
189 used as illustrated in Fig. (1). Waves with incident wave steepnesses  $H_0/L_0 =$   
190 0.075, 0.070, 0.063, 0.059, 0.055, corresponding to wave heights of  $H_1 = 1.54$  m,  
191  $H_2 = 1.44$  m,  $H_3 = 1.30$  m,  $H_4 = 1.23$  m and  $H_5 = 1.13$  m are generated to  
192 study the breaking wave forces on a vertical cylinder for different wave impact  
193 scenarios.



194 *3.2. Validation of the numerical model for breaking wave force calculation*

195 The numerical results for breaking wave forces and the free surface elevation  
196 along the frontline of the cylinder ( $x = 43.65$  m) near the tank wall for  $H_3 = 1.30$   
197 m are compared to the experimental data to validate the numerical model.  
198 The cylinder is placed with its axis at the top of the slope ( $x = 44.00$  m),  
199 such that the front surface of the cylinder is directly at the breaking point  
200 and the vertical breaking wave crest impacts the cylinder front surface. A grid  
201 size of  $dx = 0.05$  m is used. The filtered and Empirical Mode Decomposition  
202 (EMD)-treated experimental data from the experiments carried out at GWK,  
203 Hannover (Irschik et al., 2002), presented by Choi et al. (2015) is used for the  
204 comparison with the numerical results for the wave force. Figure (2a) shows  
205 that the numerical model provides a good prediction of the breaking wave force  
206 and the calculated wave force is consistent over several wave periods. Since  
207 the wave impact is very sensitive to the wave breaking location, the consistent  
208 results indicate that the model simulates successive breaking waves at the same  
209 location consistently. The numerically calculated free surface elevation along  
210 the frontline of the cylinder at  $x = 43.65$  m also presents a good agreement  
211 with the experimental data in Fig. (2b) showing that the model provides a good  
212 representation of wave breaking in the wave tank.

213 A grid convergence study is carried out by repeating the above simulation  
214 with grid sizes of  $dx = 0.20$  m,  $0.15$  m,  $0.10$  m,  $0.025$  m and compared to the  
215 results at  $dx = 0.05$  m and experimental data for the wave force in Fig. (3).  
216 The results in Fig. (3a) show that the numerical values for the wave force at  
217  $dx = 0.025$  m and  $dx = 0.05$  m converge to the experimental value. There  
218 is no significant improvement in the results for the wave forces when the grid  
219 size is improved from  $dx = 0.05$  m to  $dx = 0.025$  m. Figure (3b) shows the  
220 free surface elevation evaluated for the different grid sizes and for  $dx = 0.15$   
221 m and  $0.20$  m, neither the breaking location nor the vertical breaking crest  
222 is represented with sufficient accuracy. The wave forces calculated at these  
223 grid sizes are subsequently much lower as seen in Fig. (3a). At a grid size of  
224  $dx = 0.10$  m, the free surface differs slightly with regards to the breaking wave

225 height but the corresponding difference in the calculated wave force is large.  
 226 The vertical profile of the wave crest at breaking and the breaker location at  
 227  $t = 24.3$  s is best represented by  $dx = 0.05$  m. The horizontal and vertical  
 228 components of the water particle velocity,  $u$  and  $w$  respectively, are calculated  
 229 close to the wall along the frontline of the cylinder. The variation of  $u$  and  $w$   
 230 over time calculated on different grid sizes is presented in Figs. (3c) and (3d)  
 231 respectively. It is seen that the water particle velocities converge for  $dx = 0.05$   
 232 m. From the grid convergence studies, the grid size  $dx = 0.05$  m is selected for  
 233 all the simulations in this study. The breaking wave interaction in the numerical  
 234 wave tank for the finest grid  $dx = 0.025$  m with a total of 121 million cells is  
 235 presented in Fig. (4). The high resolution simulation does provide more detailed  
 236 flow features associated with the breaking process and the interaction with the  
 237 cylinder, but the wave forces calculated on the cylinder are seen to be the same  
 238 as that obtained using  $dx = 0.05$  m.

### 239 *3.3. Breaking wave characteristics*

240 The characteristics of wave breaking for incident waves with period  $T = 4.0$   
 241 s, wavelength  $L = 20.53$  m and heights  $H_1 = 1.54$  m,  $H_2 = 1.44$  m,  $H_3 = 1.30$   
 242 m,  $H_4 = 1.23$  m and  $H_5 = 1.13$  m is studied in a two-dimensional wave tank to  
 243 identify the various stages of wave breaking. The results are used to select the  
 244 locations to place the cylinder in order to analyse the effect of the wave breaker  
 245 location on the wave force acting on the cylinder.

246 Similarly, simulations are carried out for the other incident waves simulated  
 247 in this study and the breaking wave kinematics are analysed. The breaking  
 248 point, the breaker depth index, the breaker height index and the breaking celerity  
 249 are presented in Table (1). As the wave height decreases, waves break farther  
 250 shoreward with relatively larger increase in the wave height at breaking ( $H_b$ )  
 251 and the breaker depth index  $\gamma_b$  decreases. The waves break over the slope for  
 252  $H_1$  and  $H_2$  at the end of the slope for  $H_3$  and on the flatbed for  $H_4$  and  $H_5$ .  
 253 Further, the value of the breaker height index  $\Omega_b$  is almost 1.1 for all cases, im-  
 254 plying that the wave height evolution is not strongly influenced by the incident

255 wave characteristics.

256 Figure (5) depicts the free surface deformation and the evolution of the over-  
257 turning wave crest of the plunging breaking waves over the slope along with the  
258 horizontal velocity contours for  $H_3 = 1.30$  m. As a result of wave shoaling over  
259 the slope, the front face of the wave crest becomes steeper and the wave crest  
260 approaches a near-vertical profile in Fig. (5a). Due to increasing water particle  
261 velocities at the wave crest and reducing particle velocities towards the bed,  
262 the wave becomes asymmetrical and a part of the wave crest develops into an  
263 overturning crest seen in Fig. (5b). On further propagation, the overturning  
264 crest develops into a plunging jet which impinges the preceding wave trough,  
265 creating an air pocket, splash-up and secondary waves shorewards. The break-  
266 ing characteristics vary depending on the incident wave characteristics, which  
267 determine the size and flow features of the overturning wave crest as seen in  
268 Figs. (5d-5f).

#### 269 *3.4. Influence of cylinder location with respect to the breaker location*

270 From the study about the breaking wave process for the five incident waves  
271 in section 3.3, five different locations at different stages of wave breaking are  
272 selected, similar to the loading cases identified in Irschik et al. (2002), as follows:

- 273 A. the wave breaks behind the cylinder, the crest is not yet vertical at impact.
- 274 B. the wave breaks exactly on the cylinder, the crest is vertical at impact.
- 275 C. the wave breaks just in front of the cylinder, the overturning wave crest  
276 impacts the cylinder at crest level
- 277 D. the wave breaks in front of the cylinder, the overturning wave crest impacts  
278 the cylinder slightly below the crest level
- 279 E. the wave breaks much before the cylinder, the overturning wave crest  
280 impacts the cylinder much below the crest level.

The different scenarios are illustrated in Fig. (6). An overview of the simulations carried out for the five different incident heights and the five different wave impact scenarios is listed in Table (2). The relative distance of the front surface

of the cylinder from the breaking point is defined as

$$\tilde{x} = \frac{x_{cyl} - x_0}{L} \quad (9)$$

281 where  $x_{cyl}$  is the position of the front surface of the cylinder,  $x_0$  is the wave  
282 breaking point and  $L$  is the incident wavelength. The values of  $\tilde{x}$  and the  
283 corresponding calculated maximum breaking wave force for each simulation is  
284 presented in Table (2).

285 The calculated wave force on the cylinder in the different wave impact sce-  
286 narios for different incident wave heights is presented in Fig. (7). The maximum  
287 breaking wave force for every incident wave height is generally obtained for the  
288 scenario D, where the overturning wave crest impacts the cylinder just below  
289 the wave crest. For incident wave height  $H_1 = 1.54$  m, the maximum breaking  
290 wave force is calculated in scenario C where the overturning wave crest impacts  
291 the cylinder at crest level. This is justified as the impact scenarios C and D are  
292 close to each other. The maximum breaking wave force is calculated for these  
293 scenarios as the a large mass of water accelerating due to overturning of the  
294 wave crest impacts the cylinder surface. The lowest wave force is calculated in  
295 scenario A, where a steep non-breaking wave is incident on the cylinder surface.  
296 These findings are in agreement with previous studies for focussed waves and  
297 periodic waves (Wienke et al., 2000; Irschik et al., 2002).

298 The shape of the breaking wave force vs time plots are seen to be similar for  
299 a particular wave impact scenario for all the incident wave heights. In this case,  
300 the wave has not yet reached its breaking point and thus the impact scenario  
301 is different from the impact of an overturning wave crest. In scenario A, the  
302 wave force vs time plot does not have a distinctive peak due to the impact of  
303 the overturning wave crest. On the other hand, in case E, where the water mass  
304 from the broken wave crest and the trailing water mass impact the cylinder  
305 in succession, the breaking wave force plot shows a smaller peak just after the  
306 maximum force. The second peak results from the impact of the water mass  
307 that trails the overturning wave crest.

308 The variation of the maximum breaking wave forces with the relative dis-  
 309 tance of the cylinder from the wave breaking point ( $\tilde{x}$ ) for the different incident  
 310 waves is presented in Fig. (8a). It is seen that the breaking wave force on the  
 311 cylinder for each incident wave increases as the cylinder is moved from before the  
 312 wave breaking point to the position where the overturning wave crest impacts  
 313 the cylinder just below the wave crest. The breaking wave force is reduced when  
 314 the cylinder is moved further away from the breaking point and the overturning  
 315 wave crest impacts the cylinder much below the wave crest level for every inci-  
 316 dent wave height. The dependence of the maximum breaking wave force on the  
 317 relative distance  $\tilde{x}$  is reduced as the incident wave height  $H$  is reduced for  $\tilde{x} > 0$ .  
 318 For  $H_1 = 1.54$  m, the maximum force at  $\tilde{x} = 0.02$  is about 25% higher than the  
 319 maximum force at  $\tilde{x} = 0.16$ . Whereas for  $H_5 = 1.13$  m, the the maximum force  
 320 at  $\tilde{x} = 0.06$  is only 1.5% higher than the maximum force at  $\tilde{x} = 0.12$ .

321 The variation of the maximum wave breaking force in the different scenarios  
 322 of wave impact for the different incident wave heights is shown in Fig. (8b). Here,  
 323 it is clearly seen that the wave force is increased with increasing incident wave  
 324 height for every wave impact scenario. The maximum wave forces in scenario  
 325 A are the lowest for all the incident wave heights and the highest for scenario  
 326 D. For scenario A, where a steep non-breaking wave impacts the cylinder, the  
 327 increase in the maximum wave force as  $H$  is increased from 1.13 m to 1.54 m is  
 328 38%. For scenarios B, C and D where the the overturning wave crest impacts  
 329 the cylinder the maximum breaking wave forces increases by 62 – 80%. In the  
 330 case of scenario E, where a fully developed overturning wave crest impacts the  
 331 cylinder just before splash up, the increase in the maximum wave forces in just  
 332 27%.

333 In order to further analyse the breaking wave force characteristics, the rise  
 334 time ( $t_r$ ) is calculated for the different breaking scenarios and presented in  
 335 Fig. (9). The relative rise times are obtained by normalised the values with the  
 336 total duration of the wave impact in each case. The relative rise times ( $t_r/t_d$ )  
 337 for the different incident wave heights over different wave impact scenarios are  
 338 presented in Fig. (9a). The highest relative rise times are calculated for the

339 the lowest wave height simulated,  $H_5 = 1.13$  m, while the lowest relative rise  
340 times are calculated for the highest wave height simulated,  $H_1 = 1.54$  m. This  
341 suggests that a shorter relative rise time in the wave force plot leads to a higher  
342 breaking wave force. The relative rise time is strongly influenced by  $\tilde{x}$  for the  
343 higher incident wave heights and  $t_r$  reduces as  $\tilde{x}$  increases.

344 Figure (9b) shows the variation of the relative rise times over the incident  
345 wave height for different wave impact scenarios. Scenario A, where a steep wave  
346 impacts the cylinder before the onset of wave breaking has the highest relative  
347 rise times for every incident wave height simulated and  $t_r$  is about 55 – 58% of  
348 the total duration. The lowest rise times are calculated for scenario E, where a  
349 broken wave impacts the cylinder, with  $t_r$  being 34 – 50% of the total duration.  
350 It is noted that though the relative rise times are small, the breaking wave forces  
351 calculated for this scenario are quite low as seen in Fig. (8b). Scenario D, the  
352 scenario where the highest breaking wave forces are obtained has the second  
353 lowest relative rise times and  $t_r$  is about 55 – 34% of the total duration. This  
354 observation can be justified as follows. The breaking wave forces are generally  
355 higher when the relative rise times are lower. An exception is observed when the  
356 wave impact on the cylinder is due to a fully developed overturning wave crest  
357 in scenario E. The wave impact occurs when the overturning wave crest is about  
358 to rejoin the preceding wave crest and just before the splash up phenomenon  
359 after wave breaking. This leads to a longer total duration of the impact and  
360 thus the values of relative rise times are lower. The water mass impacting the  
361 cylinder is also lower in scenario E compared to scenario D and thus the resulting  
362 maximum breaking wave forces are lower.

363 In order to obtain more insight into the difference in the physical free surface  
364 features in two different wave impact scenarios, the breaking wave interaction  
365 with the cylinder in 3B and 3E are presented and the free surface features are  
366 discussed. Figure (10) presents the interaction process for case 3B, where the  
367 wave impacts the cylinder at the breaker location with both isometric view of  
368 the tank and the top view around the cylinder. The wave crest front profile  
369 is vertical during incidence on the cylinder front surface in Fig. (10a). The

370 wave crest begins to overturn as it passes the cylinder in Figs. (10c and 10d).  
371 The separation of the incident wavefront by the cylinder and the generation of  
372 semi-circular waves meeting in the shadow zone behind the cylinder is seen in  
373 Fig. (10d). The meeting of the semi-circular wavefronts behind the cylinder and  
374 the formation of a chute-like jet is seen in Fig. (10f). The chute-like jet originates  
375 in the region of low horizontal velocities behind the cylinder and has a maximum  
376 horizontal velocities at the tip, where it meets the broken wave crest. Figure  
377 (10g) shows the fully developed chute-like jet and is seen to extend up to just  
378 behind the broken wave crest in Fig. (10h). The chute-like jet appears after the  
379 peak force is observed for the cylinder and thus may not have a significant effect  
380 on the forces experienced by the cylinder. The importance of the chute-like jet  
381 may be more apparent in the case of neighboring cylinders placed in the zone  
382 of influence of the chute-like jet behind the first cylinder. The chute-like jet can  
383 lead to a large wave run-up on the downstream cylinder. It can also result in  
384 interaction effects between the cylinders based on the distance between the two  
385 cylinders, influencing the wave forces on both cylinders.

386 The free surface features associated with the breaking wave interaction in  
387 case 3E is presented in Fig. (11) shows the interaction of a fully developed over-  
388 turning wave crest with the cylinder. The highly curled wave crest impacts the  
389 cylinder much below the wave crest level in Fig. (11a). Figure (11c) shows the  
390 separation of the incident wavefront. Semi-circular wavefronts meeting behind  
391 the cylinder seen for 3B is not seen in here in Fig. (11d). The broken wave  
392 separated around the cylinder propagates further with a region of low velocity  
393 in the shadow region behind the cylinder in Fig. (11e). There are no major free  
394 surface features at this stage in Fig. (11f). A mildly developed chute-like jet is  
395 seen in Fig. (11g) which is close to its collapse state and this weakly developed  
396 chute wave is seen to rejoin the free surface at some distance behind the broken  
397 wave crest in Fig. (11h).

398 From the two different wave impact scenarios presented, the wave interaction  
399 process with the cylinder varies for the two cases in terms of free surface features  
400 and the velocities around the cylinder. When the wave impacts the cylinder at

401 its breaking point, in case 3B, major free surface features are noticed in the  
402 shadow region behind the cylinder, with the development of a strong chute-  
403 like jet which extends up to the broken wave crest. Semi-circular waves are  
404 formed just behind the cylinder, which meet in the shadow region and result  
405 in the chute-like jet. When the overturning wave impacts the cylinder with the  
406 overturning wave crest much below the wave crest in case 3E, the separation of  
407 the wavefront occurs without major free surface features in the region behind  
408 the cylinder. The chute-like jet is developed at a late stage is also seen to be  
409 weaker than in the previous scenario with regards to both the velocity of the  
410 chute tip and the length of extension.

#### 411 **4. Conclusions**

412 The open-source CFD model REEF3D is used to simulate breaking wave  
413 interaction with a vertical cylinder. The effect of different incident wave heights  
414 and different wave impact scenarios for each incident wave height is studied by  
415 changing the location of the cylinder. The process of wave breaking is first stud-  
416 ied using two-dimensional simulations. The cylinder locations for different wave  
417 impact scenarios are identified from these simulations. The numerical results  
418 for the wave force and the free surface elevation are compared to experimental  
419 data from large scale tests carried out at the Large Wave Channel, Hannover,  
420 Germany and a good agreement is obtained. The following conclusions can be  
421 drawn from the studies carried out in this study:

- 422 • The location of the cylinder with respect to the wave breaking point has  
423 a large influence on the breaking wave forces. This influence is more  
424 significant for higher incident waves.
- 425 • The highest force is generally seen in the scenario where the overturning  
426 wave crest impacts the cylinder just below the wave crest level and the  
427 lowest force is obtained when the wave breaks behind the cylinder.
- 428 • The breaking wave force is generally seen to be higher when the rise time



429 relative to the total duration of impact is lower. An exception is seen when  
430 a fully developed overturning wave crest impacts the cylinder, where the  
431 wave forces are lower in spite of lower relative rise times.

432 • The relative rise time is strongly influenced by the location of the cylinder  
433 with respect to the breaking point for higher incident wave heights. The  
434 relative rise time and the distance of the cylinder from the breaking point  
435 are inversely related.

436 • Different free surface features are observed in the different scenarios pre-  
437 sented. The formation of a chute-like jet is seen in the shadow region be-  
438 hind the cylinder, where the wavefront split by the cylinder partly reunites.  
439 The chute-like jet is less developed and extends to a smaller distance when  
440 the wave impacts the cylinder at a later stage of breaking.

441 The current study has presented several interesting results for breaking wave  
442 interaction with vertical slender cylinders. The results can be used to extend the  
443 knowledge regarding breaking wave forces to the complex scenario of breaking  
444 wave interaction with tripod and truss structures.

#### 445 **Acknowledgements**

446 This study has been carried out under the OWCBW project (No. 217622/E20)  
447 and the authors are grateful to the grants provided by the Research Council of  
448 Norway. This study was supported in part with computational resources at the  
449 Norwegian University of Science and Technology (NTNU) provided by NOTUR,  
450 <http://www.notur.no> (NN2620K).

451 Alagan Chella, M., Bihs, H., Myrhaug, D., 2015a. Characteristics and profile  
452 asymmetry properties of waves breaking over an impermeable submerged reef.  
453 Coastal Engineering 100, 26–36.

454 Alagan Chella, M., Bihs, H., Myrhaug, D., Muskulus, M., 2015b. Breaking char-  
455 acteristics and geometric properties of spilling breakers over slopes. Coastal  
456 Engineering 95, 4–19.

- 457 Alagan Chella, M., Bihs, H., Myrhaug, D., Muskulus, M., 2015c. Hydrodynamic  
458 characteristics and geometric properties of plunging and spilling breakers over  
459 impermeable slopes. *Ocean Modelling*, Virtual Special Issue: Ocean Surface  
460 Waves , 1–20.
- 461 Arntsen, Ø.A., Ros, X., Tørum, A., 2011. Impact forces on a vertical pile from  
462 plunging breaking waves, in: *Coastal Structures*.
- 463 Berthelsen, P.A., Faltinsen, O.M., 2008. A local directional ghost cell approach  
464 for incompressible viscous flow problems with irregular boundaries. *Journal*  
465 *of Computational Physics* 227, 4354–4397.
- 466 Bihs, H., Kamath, A., Alagan Chella, M., Aggarwal, A., Arntsen, Ø.A., 2016.  
467 A new level set numerical wave tank with improved density interpolation for  
468 complex wave hydrodynamics. *Computers & Fluids* .
- 469 Bradshaw, P., Ferriss, D.H., Atwell, N.P., 1967. Calculation of boundary layer  
470 development using the turbulent energy equation. *Journal of Fluid Mechanics*  
471 28, 593–616.
- 472 Bredmose, H., Jacobsen, N.G., 2010. Breaking wave impacts on offshore wind  
473 turbine foundations: focused wave groups and CFD. *Proc., 29th International*  
474 *Conference on Ocean, Offshore and Arctic Engineering*, Shanghai, China .
- 475 Bullock, G.N., Obhrai, C., Peregrine, D.H., Bredmose, H., 2007. Violent break-  
476 ing wave impacts. part 1: Results from large-scale regular wave tests on ver-  
477 tical and sloping walls. *Coastal Engineering* 54, 602–617.
- 478 Chan, E.S., Melville, W.K., 1988. Deep-water plunging wave pressures on a  
479 vertical plane wall, in: *Proc. of the Royal Society of London. A. Mathematical*  
480 *and Physical Sciences*, pp. 95–131.
- 481 Choi, S.J., Lee, K.H., Gudmestad, O.T., 2015. The effect of dynamic am-  
482 plification due to a structure s vibration on breaking wave impact. *Ocean*  
483 *Engineering* 96, 8–20.

- 484 Chorin, A., 1968. Numerical solution of the Navier-Stokes equations. *Mathe-*  
485 *matics of Computation* 22, 745–762.
- 486 Durbin, P.A., 2009. Limiters and wall treatments in applied turbulence model-  
487 ing. *Fluid Dynamics Research* 41, 1–18.
- 488 Goda, Y., Haranaka, S., Kitahata, M., 1966. Study on impulsive breaking wave  
489 forces on piles. Report Port and Harbour Technical Research Institute 6,  
490 1–30.
- 491 Irschik, K., Sparboom, U., Oumeraci, H., 2002. Breaking wave characteristics  
492 for the loading of a slender pile, in: Proc. 28th International Conference on  
493 Coastal Engineering, Cardiff, Wales.
- 494 Jacobsen, N.G., Fuhrman, D.R., Fredsøe, J., 2012. A wave generation toolbox  
495 for the open-source CFD library: OpenFOAM. *International Journal for*  
496 *Numerical Methods in Fluids* 70, 1073–1088.
- 497 Jiang, G.S., Peng, D., 2000. Weighted ENO schemes for Hamilton-Jacobi equa-  
498 tions. *SIAM Journal on Scientific Computing* 21, 2126–2143.
- 499 Jiang, G.S., Shu, C.W., 1996. Efficient implementation of weighted ENO  
500 schemes. *Journal of Computational Physics* 126, 202–228.
- 501 Larsen, J., Dancy, H., 1983. Open boundaries in short wave simulations - a new  
502 approach. *Coastal Engineering* 7, 285–297.
- 503 Lin, P., Liu, P.L.F., 1998. A numerical study of breaking waves in the surf zone.  
504 *Journal of Fluid Mechanics* 359, 239–264.
- 505 Mo, W., Jensen, A., Liu, P.L.F., 2013. Plunging solitary wave and its interaction  
506 with a slender cylinder on a sloping beach. *Ocean Engineering* 74, 48–60.
- 507 Morison, J.R., O’Brien, M.P., Johnson, J.W., Schaaf, S.A., 1950. Force exerted  
508 by surface waves on piles. *Journal of Petroleum Technology* 2, 149–154.

- 509 Naot, D., Rodi, W., 1982. Calculation of secondary currents in channel flow.  
510 Journal of the Hydraulic Division, ASCE 108, 948–968.
- 511 NOTUR, 2012. The Norwegian Metacenter for Computational Science.  
512 <http://www.notur.no/hardware/vilje> .
- 513 Osher, S., Sethian, J.A., 1988. Fronts propagating with curvature- dependent  
514 speed: algorithms based on Hamilton-Jacobi formulations. Journal of Com-  
515 putational Physics 79, 12–49.
- 516 Peng, D., Merriman, B., Osher, S., Zhao, H., Kang, M., 1999. A PDE-based  
517 fast local level set method. Journal of Computational Physics 155, 410–438.
- 518 Schäffer, H.A., Klopman, G., 2000. Review of multidirectional active wave  
519 absorption methods. Journal of Waterway, Port, Coastal, and Ocean Engi-  
520 neering 126, 88–97.
- 521 Shu, C.W., Osher, S., 1988. Efficient implementation of essentially non-  
522 oscillatory shock capturing schemes. Journal of Computational Physics 77,  
523 439–471.
- 524 Sumer, B.M., Fredsøe, J., 1997. Hydrodynamics around cylindrical structures.  
525 Vol. 12, World Scientific.
- 526 van der Vorst, H., 1992. BiCGStab: A fast and smoothly converging variant  
527 of Bi-CG for the solution of nonsymmetric linear systems. SIAM Journal on  
528 Scientific and Statistical Computing 13, 631–644.
- 529 Wienke, J., Oumeraci, H., 2005. Breaking wave impact force on a vertical and  
530 inclined slender pile – theoretical and large-scale model investigations. Coastal  
531 Engineering 52, 435–462.
- 532 Wienke, J., Sparboom, U., Oumeraci, H., 2000. Breaking wave impact on a  
533 slender cylinder, in: Coastal Engineering Conference, pp. 1787–1798.
- 534 Wilcox, D.C., 1994. Turbulence modeling for CFD. DCW Industries Inc., La  
535 Canada, California.

<sup>536</sup> Zhao, Q., Armfield, S., Tanimoto, K., 2004. Numerical simulation of breaking  
<sup>537</sup> waves by a multi-scale turbulence model. *Coastal Engineering* 51, 53–80.

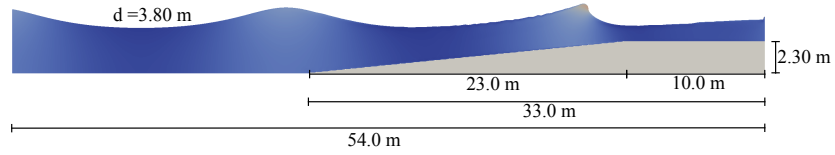
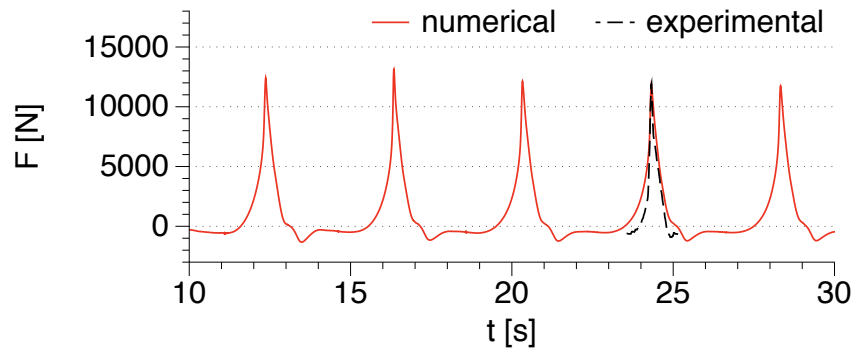
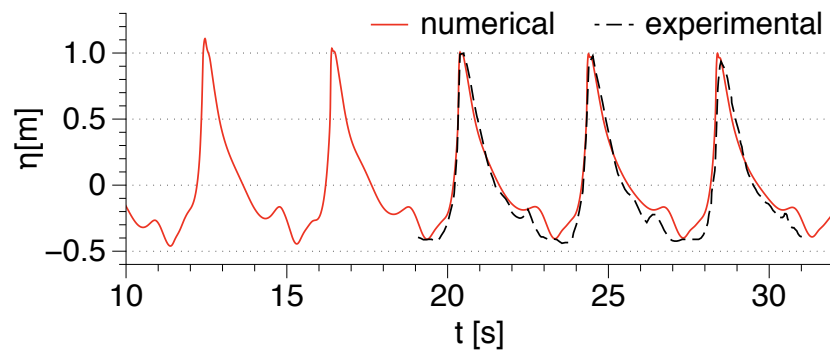


Figure 1: Dimensions of the two-dimensional numerical wave tank to determine breaking wave characteristics



(a) wave force on the cylinder



(b) free surface elevation at the tank wall, along the frontline of the cylinder

Figure 2: Comparison of numerical results with experimental data

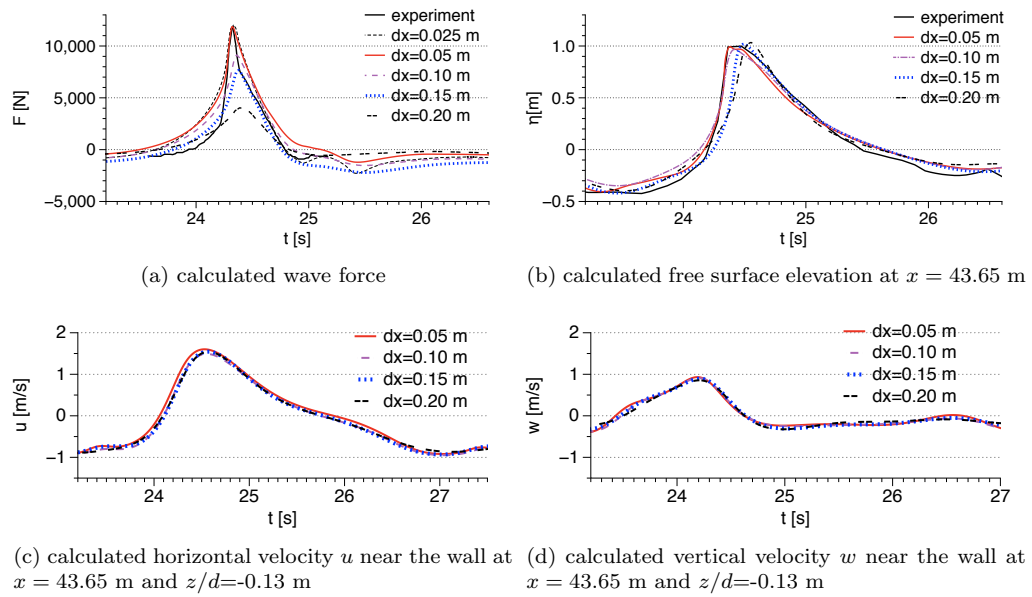


Figure 3: Grid convergence study for wave forces and free surface elevation near the wall along the frontline of the cylinder

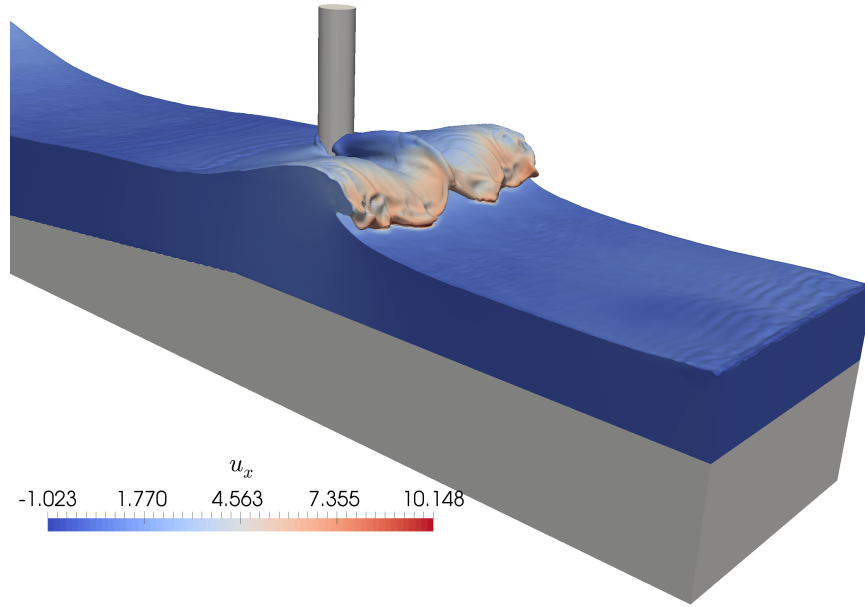


Figure 4: Breaking wave interaction with a vertical cylinder in the numerical wave tank with  $dx = 0.025$  m and a total of 121 million cells showing the horizontal velocity contours

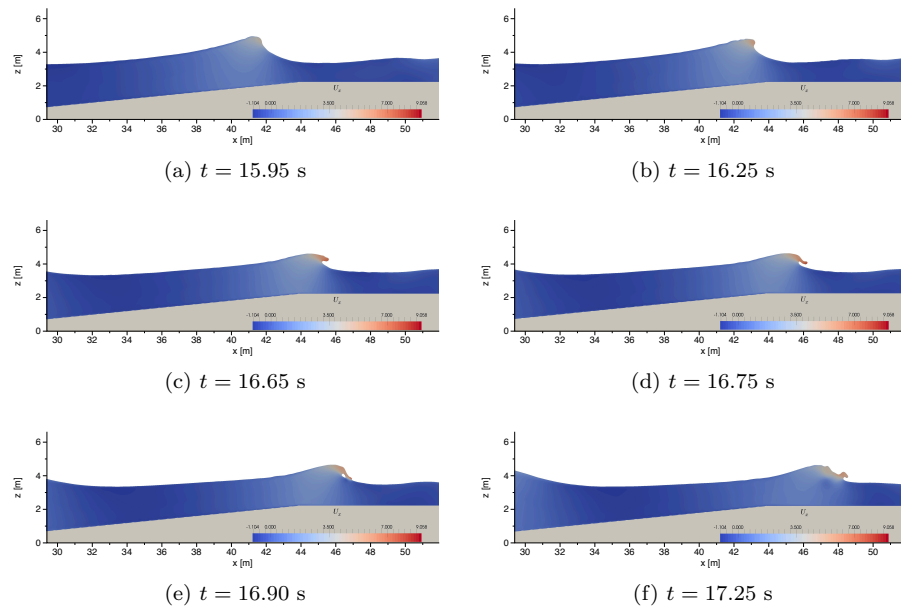


Figure 5: Evolution of the breaking wave for  $H_B = 1.30$  m with horizontal velocity contours



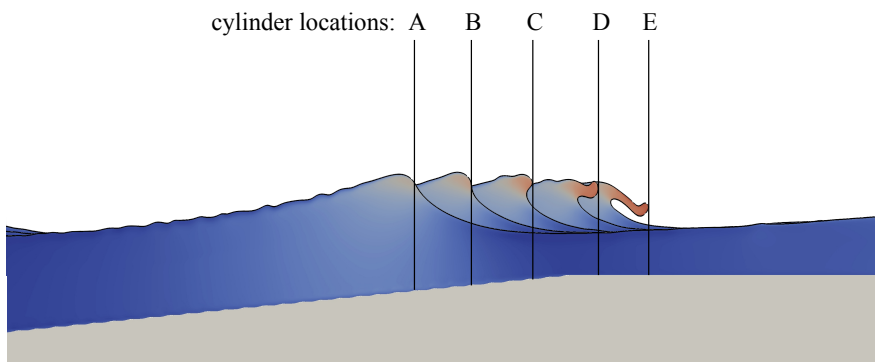


Figure 6: Location of the cylinder front surface for various wave loading cases

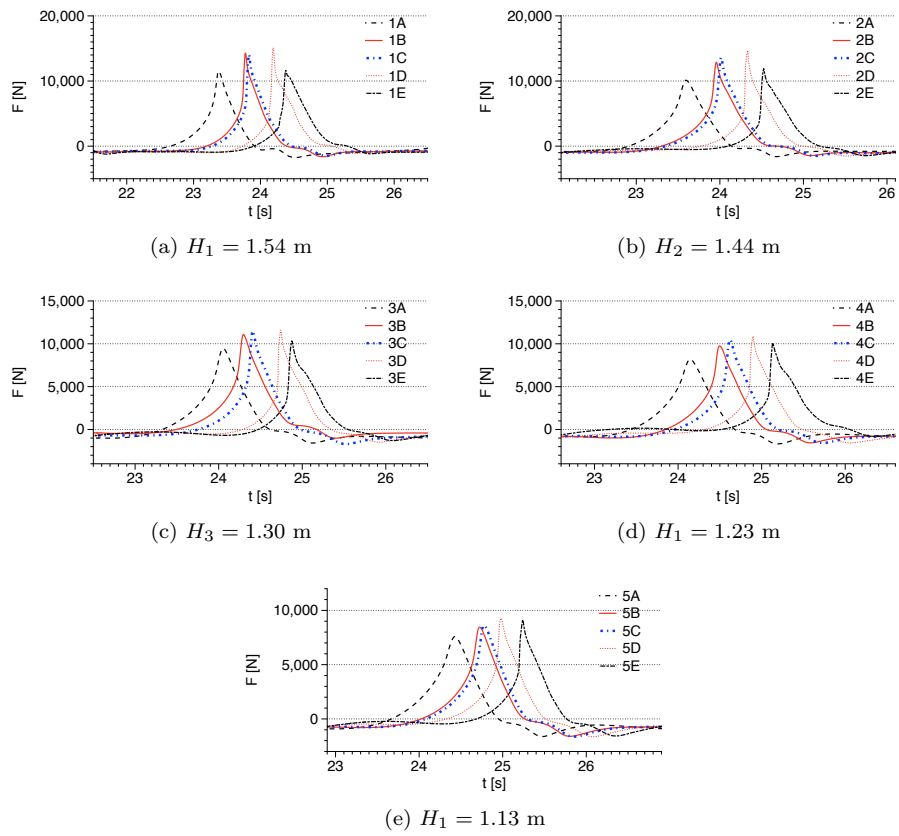
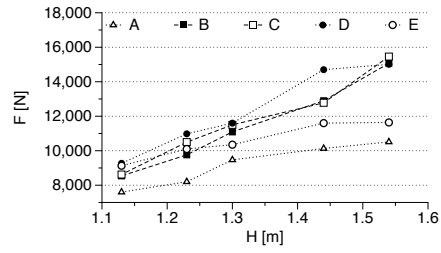
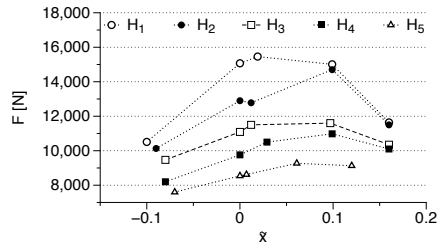


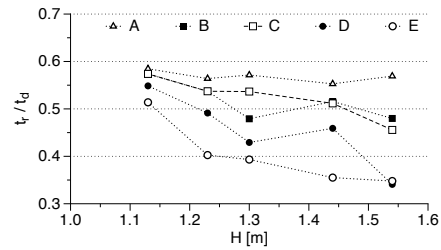
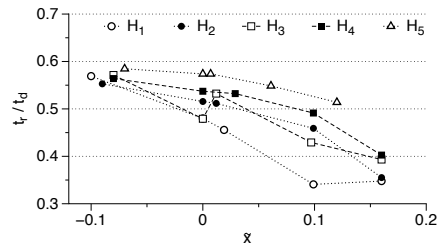
Figure 7: Breaking wave forces in different scenarios A-E for different incident wave heights  $H_1 - H_5$



(a) variation of maximum breaking wave force with distance from breaking point for different incident wave heights

(b) variation of maximum breaking wave force with wave height for various impact scenarios

Figure 8: Variation of the maximum breaking wave force with distance of cylinder front surface from the wave breaking point



(a) variation of maximum breaking wave force with distance from breaking point for different incident wave heights

(b) variation of maximum breaking wave force with wave height for various impact scenarios

Figure 9: Variation of breaking wave force rise time and total time of impact in the different scenarios

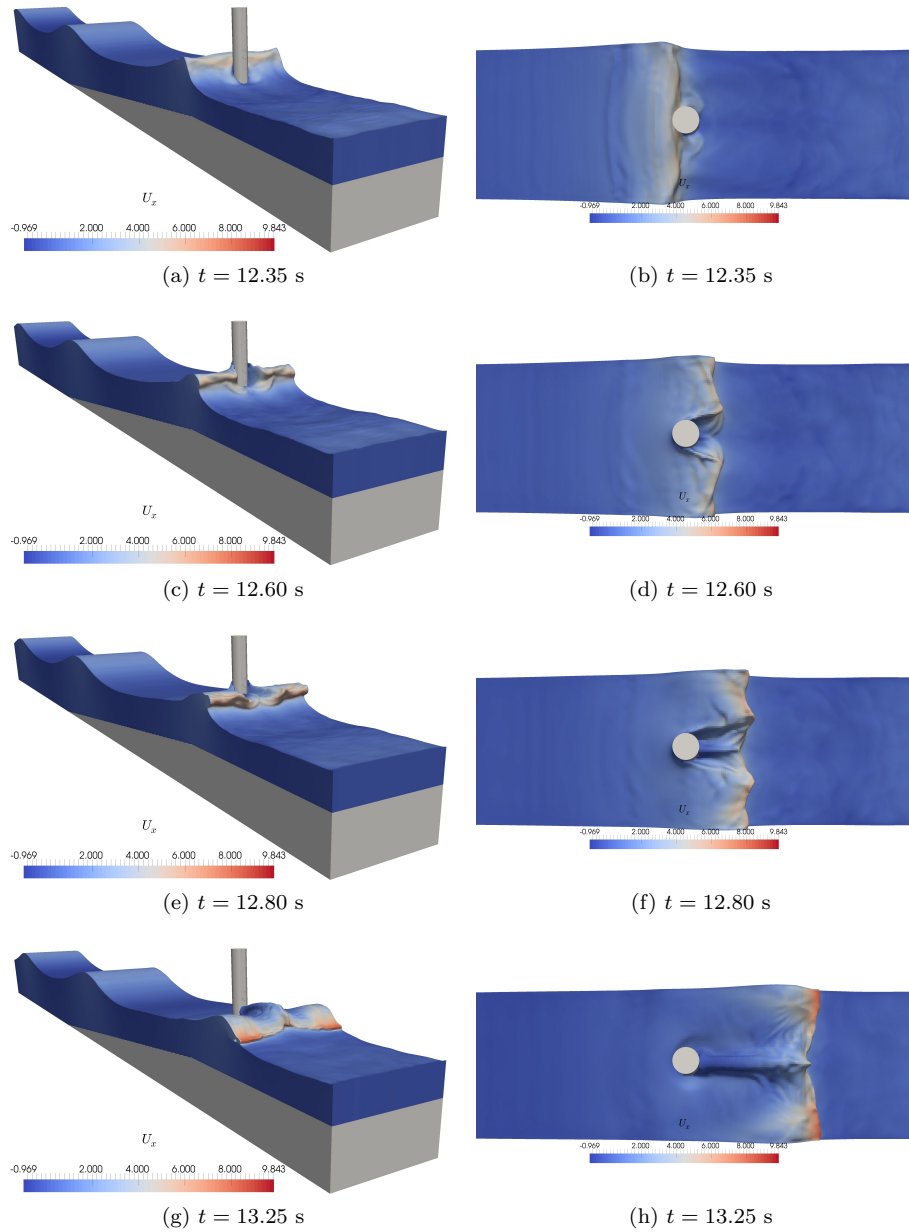


Figure 10: Isometric and corresponding top views of breaking wave interaction with the cylinder for  $H_B = 1.30$  m for scenario 3B

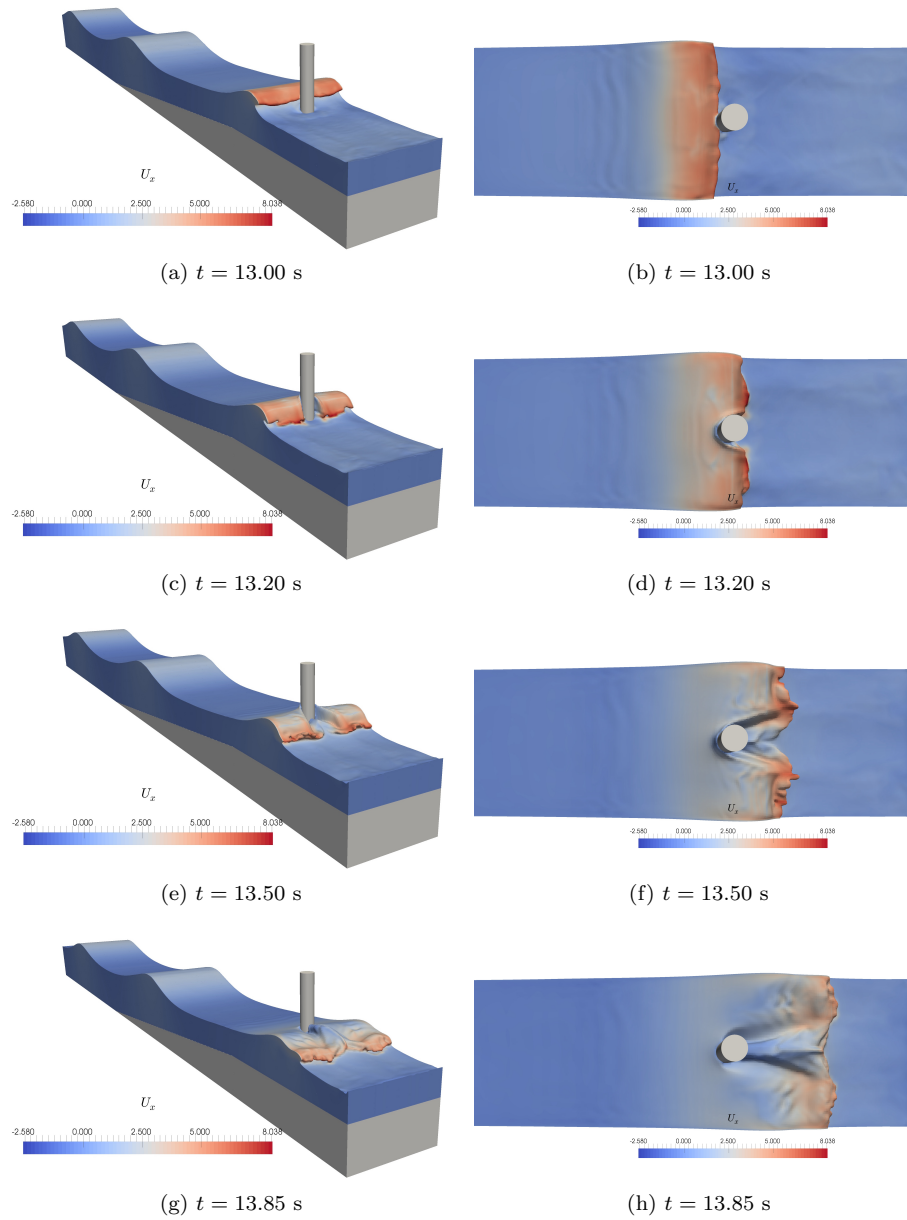


Figure 11: Isometric and corresponding top views of breaking wave interaction with the cylinder for  $H_B = 1.30$  m for scenario 3E

No.	incident wave height, $H$ (m)	breaker height $H_b(m)$	breaking point $x_b$ (m)	breaker depth index, $\gamma_b$	breaker height index, $\Omega_b$
$H_1$	1.54	1.68	42.05	0.991	1.09
$H_2$	1.44	1.55	42.45	0.936	1.08
$H_3$	1.30	1.44	43.65	0.938	1.10
$H_4$	1.23	1.32	44.20	0.880	1.07
$H_5$	1.13	1.27	45.00	0.846	1.12

Table 1: Overview of the five different incident wave heights simulated and related breaking wave kinematics

No.	H (m)	$x_b$ (m)	Cylinder axis (m)	$\tilde{x}$	F [N]
1A	1.54	42.05	40.35	-0.10	10510
1B			42.40	0.0	15070
1C			42.65	0.012	15460
1D			44.45	0.10	15010
1E			45.70	0.16	11520
2A	1.44	42.45	40.95	-0.09	10130
2B			42.80	0.0	12900
2C			43.05	0.012	12780
2D			44.85	0.10	14700
2E			46.25	0.16	10050
3A	1.30	43.65	42.70	-0.08	9470
3B			44.00	0.0	11090
3C			44.60	0.012	11500
3D			46.35	0.097	11600
3E			47.35	0.16	7580
4A	1.23	44.20	42.85	-0.08	8200
4B			44.55	0.0	9760
4C			45.15	0.03	10500
4D			46.60	0.10	10980
4E			47.85	0.16	10100
5A	1.13	45.00	43.80	-0.07	7600
5B			45.35	0.0	8540
5C			45.50	0.007	8620
5D			46.60	0.06	9270
5E			47.80	0.12	9130

Table 2: Overview of the simulations carried out to investigate the effect of different breaking wave impact scenarios